

Observation of strong helical excitons and unexpectedly giant Rashba splitting in single crystal two-dimensional Organic-Inorganic Halide Perovskites

Andrivo Rusydi (✉ phyandri@nus.edu.sg)

National University of Singapore

Xiao Chi

National University of Singapore

Kai Leng

Department of Applied Physics, The Hong Kong Polytechnic University

Runlai Li

Department of Chemistry, National University of Singapore

Xiaojiang Yu

Singapore Synchrotron Light Source, National University of Singapore

Ping Yang

National University of Singapore

Mark Breese

National University of Singapore

Kian Ping Loh

Department of Chemistry, National University of Singapore, 3 Science Drive 3, Singapore 117543.

<https://orcid.org/0000-0002-1491-743X>

Physical Sciences - Article

Keywords: Spin-orbit Coupling, Broken Inversion Symmetry, Quantum Well Thickness, Surface Inversion Asymmetry, Surface-normal Electric Fields

Posted Date: December 7th, 2020

DOI: <https://doi.org/10.21203/rs.3.rs-119349/v1>

License:  This work is licensed under a Creative Commons Attribution 4.0 International License.

[Read Full License](#)

Observation of strong helical excitons and unexpectedly giant Rashba splitting in single crystal two-dimensional Organic-Inorganic Halide Perovskites

Xiao Chi^{1,2,3}, Kai Leng⁴, Runlai Li⁵, Xiaojiang Yu¹, Ping Yang¹, Mark B.H. Breese^{1,2}, Kian Ping Loh^{3,5†}, Andriwo Rusydi^{1,2,3,6‡}

¹ *Department of Physics, National University of Singapore, 117576, Singapore*

² *Singapore Synchrotron Light Source, National University of Singapore, 5 Research Link, 117603, Singapore*

³ *Centre for Advanced 2D Materials and Graphene Research Centre, National University of Singapore, 117546, Singapore*

⁴ *Department of Applied Physics, The Hong Kong Polytechnic University, Hung Hom, Kowloon, Hong Kong*

⁵ *Department of Chemistry, National University of Singapore, 3 Science Drive 3, Singapore 117543*

⁶ *NUS Graduate School for Integrative Sciences and Engineering, 117456, Singapore*

E-mail: [‡]phyandri@nus.edu.sg; [†]chmlohkp@nus.edu.sg

Abstract: Two-dimensional (2D) organic-inorganic lead halide perovskites possess strong spin-orbit coupling, and in the presence of broken inversion symmetry, this may lead to helical excitons and Rashba splitting at the band extrema¹⁻⁶. However, a direct and systematic measurement of the helical excitons and the Rashba parameter in the system is still lacking. Here, we report distinct two bright co-helical and two dark anti-helical excitons in single crystal $((\text{CH}_3(\text{CH}_2)_3\text{NH}_3)_2(\text{CH}_3\text{NH}_3)_{n-1}\text{Pb}_n\text{I}_{3n+1})$ ($n = 1$ to 4), where n determines quantum well (QW) thickness of inorganic layer⁷. By comprehensively analyzing the fine structure of helical excitons, we find that the Rashba splitting originates from surface inversion asymmetry and surface-normal electric fields, which are determined by the QW's dielectric environment, n and temperature. The Rashba splitting parameter is found among the highest recorded of 2.66 and 2.5 eV·Å for the conduction and valence band of $n=1$ Iodide, respectively, and reduces for $n>1$ Iodide. Our result shows the importance of helical excitons and Rashba splitting and presents a direct method to quantify the Rashba parameter in complex halide perovskites. We hope that our study inspires applications of QW materials in novel spintronic devices.

Introduction

Two-dimensional (2D) Ruddlesden-Popper perovskites (RPPs) are a class of quantum well (QW)-like materials represented by the formula $(R)_2(A)_{n-1}M_nX_{3n+1}$, where R and A are organic cations, M is a divalent metal cation and X is a halide anion. The value of parameter n indicates the number of the inorganic metal-halide layers between the two layers of the organic chains and determines the QW thickness^{7,8}. Therefore, the degree of quantum and dielectric confinements as well as related properties, such as band gaps⁹⁻¹², excitonic binding energies⁹ and Rashba effect⁵ are expected to vary with n . The arrangement of RPPs is fundamentally different from transition metal dichalcogenides, in which one layer of the metal ions is sandwiched between two hexagonal layers of S or Se atoms, affording a rigid backbone and dielectric environments¹³⁻¹⁵. Therefore, compared with traditional three-dimensional (3D) perovskites and classic dichalcogenide based 2D materials, RPPs offer rich new phenomena for fundamental studies and provide tremendous advantages for various applications. Recently, the synthesis of phase-pure (purified to one n value) 2D single crystal perovskites with high n values was achieved^{7,10}. This opens a new possibility to explore intrinsic physical properties, in particular the electronic structure and optical properties such as helical excitons and Rashba splitting in single crystalline RPPs.

The presence of heavy atoms such as lead and iodine introduces strong spin-orbit coupling (SOC) in the electronic structure^{1,16,17}, which makes it highly relevance to spintronics. In non-centrosymmetric crystals, or at surfaces or interfaces where inversion symmetry is broken, the electrons feel an effective electromagnetic field due to the SOC. This interaction, known as the Rashba effect^{1-4,18,19}, removes the electron spin degeneracy

and splits the corresponding valence band (VB) and conduction band (CB), resulting in various spin textures at the band edges^{2,20}. One compelling observation at the Rashba band edge is energy ordering of excitons. In particular, for 2D RPPs, helical excitons consisting of bright co-helical and dark anti-helical excitons have been predicted due to Rashba splitting (Figs. 1a and b)²⁰. Owing to the spin-pair helicities of VB and CB, each exciton state is split into several energy sublevels, known as fine structure. Therefore, finding helical excitons are crucial for fundamental understanding of electronic structure and Rashba effect in 2D RPPs.

For halide perovskites, Rashba-type effects may lead to intriguing and rich phenomena. An example is that the band shift in momentum space (k -space) may cause a direct-to-indirect band gap transition, and the shift is strongly dependent on the magnitude of Rashba splitting²⁻⁴. This has a direct consequence on the recombination dynamics of charge carriers. The Rashba effect in 3D RPPs has been studied using angle resolved photoemission spectroscopy³, photogalvanic effect^{21,22} and electro-absorption²³, but the Rashba parameters determined showed great disparity. Rashba splitting in 2D (PEA)₂PbI₄ was reported to be ~ 1.6 eV Å using a low-energy peak in the electro-absorption spectrum and attributed to transitions between the Rashba spin split bands¹⁹. However, a direct way to measure helical excitons and spin splitting at the Rashba bands (both VB and CB) is still lacking and challenging.

In this Letter, we use high-resolution and angle-dependent spectroscopic ellipsometry (SE) to directly probe electronic and optical fine structure of ((CH₃(CH₂)₃NH₃)₂(CH₃NH₃) _{n} -1Pb _{n} I_{3 n +1} ($n = 1$ to 4) and establish a relationship between the Rashba effect and the thickness of the QW through RPPs. Spectroscopic ellipsometry

is the most direct and self-normalized technique to simultaneously probe excitons and spin excitation, which have been shown successfully in transition metal oxides²⁴. We perform polarization-dependent X-ray absorption spectroscopy (XAS) measurements at the C *K*-edge to reveal the surface symmetry broken. All measurements are performed in high vacuum and all samples are fresh single crystals with surface-cleaved to avoid surface reconstruction and contamination. We reveal for the first time helical excitons, two bright co-helical and two dark anti-helical excitons in complex 2D RPPs. By analyzing the fine structure of the helical excitons as well as spectral weight transfer (SWT) at the band extrema, the dispersion relations of VB and CB extrema are determined. We find that both CB and VB present strong SOC effects. Interestingly, the Rashba effect originates from the surface inversion symmetry breaking and the Rashba splitting energies are mainly determined by the QW dielectric and confinement effects with the assistance of the formation of an internal electric field. Our result shows the observation of helical excitons and thus Rashba effect can be readily revealed by analyzing the fine structure of helical excitons from complex dielectric functions in RPPs.

Large size RPPs single crystals $((\text{CH}_3(\text{CH}_2)_3\text{NH}_3)_2(\text{CH}_3\text{NH}_3)_{n-1}\text{Pb}_n\text{I}_{3n+1})$ ($n=1$ to 4) are grown using a temperature-programmed crystallization⁷. The crystal structures and phase purity of the as-grown large-sized 2D RPPs single crystal family with $n=1$ to 4 are confirmed by synchrotron-based X-ray diffraction (XRD) (see Supplementary Note 1). Schematics of the QW-like crystal structures are shown in Supplementary Fig. S1. The diffraction patterns only show (00L) orientation for all samples (Supplementary Fig. S2), indicating a highly ordered layered stacking arrangement. The lattice constants c for $n=1$ to 4 are 13.87 Å, 19.12 Å, 25.06 Å and 31.29 Å, respectively; the increased thickness of c

corresponds to the change of QW width due to more PbI₆ sheets inserted between two organic layers (Supplementary Fig. S1). In the extreme case where $n=\infty$, the structure becomes a three-dimensional perovskite similar to BaTiO₃²⁵⁻²⁸.

The optical fine structure is the most direct and important property in revealing helical excitons²⁴ as well as Rashba splitting (c.f. Figs. 1a and b). It has been successfully used to study a variety of SOC type of materials, including a polar BiTeI semiconductor²⁹ and a Weyl semimetal³⁰. The electron dispersion relation near the CB and VB extrema points is described by the effective-mass approximation^{2,19}

$$E(k) = \hbar^2 k^2 / 2m^*, \quad (1)$$

where m^* is effective mass of carriers and k is momentum wavevector. The presence of heavy elements in the crystal gives rise to spin-orbit coupling, which, combined with the breaking of the inversion or crystal symmetry, can lift the spin-degeneracy in both momentum space and energy space and thus shift the spin band away from the symmetric points. The new electron/hole dispersion relation can be described by^{2,19}

$$E(k) = \hbar^2 k^2 / 2m^* \pm \alpha |k|, \quad (2)$$

where Rashba parameter $\alpha = 2\Delta/k_0$, k_0 is the band maximum shifted from the high symmetry point and Δ is the Rashba energy splitting (see Supplementary Note 4). For $n=1$ Iodide, we find the lowest interband transition is ~ 2.80 eV, which is also identified as an optical band gap for $n = 1$ (Figs. 1c and d).

Our main observation is huge and sharp optical features of helical excitons at ~ 2.55 (peak II) and ~ 2.57 eV (peak III) accompanied by two satellite-*like* features at ~ 2.46

(peak I) and ~ 2.62 eV (peak IV) as shown in Figs. 1c and d. Interestingly, the intensity of ϵ_2 of peaks II and III is more than 30 times than that of ϵ_2 at the band-to-band transition. Generally, an exciton excitation involves a Coulombic pairing of an electron in the conduction band with a hole in the valence band (Fig. 1a). The Rashba interactions cause these excitons to be split into multiple fine structures (Fig. 1b) and lead to an energy splitting of spin texture (counter-clockwise ($\chi=1$) and clockwise ($\chi=-1$)) at band extrema. The electron-hole interactions with spin selectivity due to excited states from the helical Rashba valence band to the helical Rashba conduction band result in either a bright co-helical exciton ($\chi_{vb} \cdot \chi_{cb}=1$) or a dark anti-helical exciton ($\chi_{vb} \cdot \chi_{cb}=-1$)². In a Rashba split 2D RPPs crystal, we clearly observe two bright co-helical excitons (peaks II and III) and two dark anti-helical excitons (peaks I and IV) at the band edges. The bright co-helical excitons correspond to the spin-allowed transitions ($V_{\chi=1} \rightarrow C_{\chi=1} / V_{\chi=-1} \rightarrow C_{\chi=-1}$) and the dark co-helical excitons are assigned to the spin-forbidden transitions. This is the first observation of the theoretically predicted multiple helical excitons in 2D RPPs. Because SE is very sensitive to spin excitations²⁴, the energy ordering and huge intensity of ϵ_1 and ϵ_2 below the interband transitions also rule out the origins of these peaks as defect or conventional excitons.

To quantitatively assess the Rashba effects on both CB and VB, we fit the fine structure for $n=1$ Iodide (Fig. 1c). The fine structure can be well-fitted with four peaks associated with bright co-helical and dark anti-helical excitons. Peak I is rather weak due to being spin-forbidden or optically inactive, implying that the spin textures at the band extrema are opposite. To support our analysis, we also measure optical fine structure for $n=1$ Bromide ($((\text{CH}_3(\text{CH}_2)_3\text{NH}_3)_2\text{PbBr}_4)$) and Chloride ($((\text{CH}_3(\text{CH}_2)_3\text{NH}_3)_2\text{PbCl}_4)$). We find

that for $n=1$ Br, Rashba splitting is considerably large, showing large SOC (Supplementary Fig. S4). While for $n=1$ Chloride, Rashba splitting reduces as evident by the two spin-forbidden transitions that cannot be well-resolved, revealing that the SOC of Cl on VB is negligible (Supplementary Fig. S5). This further demonstrates that our experimental approach provides the most direct and detailed information and roles of halide are important in determining the Rashba splitting and helical excitons in 2D RPPs.

We next study the effect of temperature on the helical excitons and Rashba splitting in $n=1$ Iodide (Figs. 2a to d). As the temperature increases up to 297 K, all four helical excitons persist. We observe a new electronic transition at ~ 230 K, in which the energy of helical excitons redshifts by ~ 160 meV. A measurement of differential calorimetric scan has shown that the crystal undergoes a phase change at ~ 223 K³¹, suggesting that there is a strong coupling between electronic and lattice degrees of freedom in this system. We fit these temperature-dependent fine structure data and the fitting parameters are summarized in Figs. 2e to h. The Rashba energy splittings Δ_{pb} and Δ_I of both CB and VB are calculated from the energy differences between spin-allowed and spin forbidden transitions, namely $E(\text{CB}) = \Delta_{pb} = E(\text{III}) - E(\text{I})$ and $E(\text{VB}) = \Delta_I = E(\text{II}) - E(\text{I})$ as a function of temperature (Fig. 2g). The following salient features are revealed; (i) The integrated intensity (spectral weight), the peak energy and the full-width at half-maximum (FWHM) of four helical excitons change dramatically at the phase transition temperature (Supplementary Note 3); (ii) the Δ_{pb} and Δ_I are only changed moderately. This shows that the change of inherent crystal structure does not play a dominant role in the Rashba splitting of $n=1$ Iodide, and instead the origin of Rashba splitting in $n=1$ Iodide is mainly from the surface inversion symmetry breaking as discussed later.

Importantly, the spectral weights of the four excitons are increased dramatically at lower temperature and uncover strong spectral weight transfers from well-above optical band gap to the helical excitons. Spectral weight transfer in wide photon energy is a fingerprint of electronic correlation³²⁻³⁵, therefore this reveals that electronic correlation plays an important role in the helical excitons. Furthermore, we also find that the role of electron-phonon interactions in which the Rashba splitting energies Δ_{pb} and Δ_I are slightly increased as temperature increases (Fig. 2g).

To reveal the role of QW's thickness on the helical excitons and Rashba splitting, we measure complex dielectric function for $n=1$ to 4 Iodides (Figs. 3a and b). The result of the helical excitons energy and Rashba splitting as a function of n are summarized in Figs. 3c and d. All samples show a considerably large Rashba splitting on both the CB and VB. The helical exciton energy and the Rashba splitting energy decrease monotonously with decreasing n from 4 to 1, which indicates a strong quantum and dielectric confinement resulting in a complex many-body interaction of electronic correlations and a large Rashba splitting (as depicted in Fig. 3e).

The Rashba splitting also has a strong correlation with the crystal symmetry and internal electric field of the QW (Supplementary Fig. S1). The crystal structure of 2D RPPs can be described in terms of a polar semiconductor model, where the long chain molecule R forms a positively charged $(R_2)^+$ layer which separates the dielectric $((A)_n-1M_nX_{3n+1})^{2-}$ layer. Thus, the crystal structure possesses a polar axis along the stacking direction and leads to a potential gradient (or electric dipole field (E_z)) at the surface due to uncompensated charges^{36,37}. The Rashba effect is directly related to the strength of the potential gradient. We argue that the strength of the potential gradient is determined by

two factors. The first factor is the QW thickness (l), as the potential gradient is inversely proportional to the QW thickness ($\alpha \propto E_z \propto Q/l$, where Q is uncompensated charges). The second factor is molecule orientation, as unordered molecule orientation could result in a pronounced polar distortion and counteract the charge dipole field, which further reduces the Rashba energy splitting. Therefore, a narrower QW with higher order of molecule at the surface would prominently increase the Rashba splitting.

The molecule orientation in both organic and inorganic frameworks can be estimated by polarization-dependent X-ray absorption spectroscopy (XAS) and linear dichroism (XLD) at carbon K edge as graphically depicted in Fig. 4a, which describes the relationship between the linear polarization of a photon and the orbital symmetries. In all cases, the interaction would become strongest when photon polarization is along the direction of the orbital lobes of carbon $2p$. Therefore, when a molecule is orderly arranged, the absorption spectra show the highest XLD signal. In contrast, there is no XLD that can be measured for a disordered molecular structure. The XLD ($I_{GI}-I_{NI}$) spectra recorded with E polarization of photon along normal (NI) and along grazing (GI) incidence for all four samples ($n=1$ to 4 Iodides) are shown in Fig. 4b. Interestingly, the XLD signal becomes weak as n increases, implying that the addition of methyl ammonium ($n>1$) introduces disorder in the system owing to its dynamic rotation and electrostatic effects.

In order to quantitatively determine the potential gradient in one unit cell of each type of sample, we perform *in situ* high-energy-resolution x-ray photoelectron spectroscopy (XPS) measurements. The binding energy separation between the elements (such as C^{4+} , Pb^{2+} and I^-) in organic and inorganic frameworks is observed to become more prominent

when increasing the internal electric dipole field (Fig. 4c). The relevant energy shift of the four samples ($n=1$ to 4 Iodides) and a 3D structure ($n=\infty$) as a reference is summarized in Figure 4d. The monotonic energy shift reveals an increased built-in potential between organic and inorganic frameworks with decrease of n , and a maximum of 0.137 eV/\AA of potential gradient can be obtained from $n=1$ Iodide. This highlights the importance of many-body interactions (such as QW confinement, dielectric and polar field) in influencing the Rashba effect in 2D RPPs.

Finally, from the Rashba splitting energies, we can readily estimate the offset, k_0 , in momentum space using a parabolic dispersion relation with an electron effective mass for both VB and CB. The electron effective mass can be obtained by the following equation:³⁸

$$E_g = E_g^{3D} + \frac{\hbar^2 \pi^2}{2\mu(L_{\text{eff}})^2} \quad (3)$$

where E_g^{3D} is the band gap of the 3D ($n=\infty$) reference material, μ is the electron and hole effective mass, and L_{eff} is the QW effective thickness. For simplification, we assume that QW effective thickness is correlated with both QW and barrier, and L_{eff} can be expressed as $A*L_{\text{QW}}+B*L_b$, where A , B and as well electron effective mass can be obtained by best fitting of equation (3) with experimental data as shown in Fig. 1e. The experimental band gap of RPPs with various QW thicknesses can be well reproduced by equation (3) and the reduced effective mass $\mu \cong 0.23m_e$ (m_e is the mass of a free electron) can be determined by this best fitting. We thus are able to obtain k_0 both at the CB and VB by using

$\Delta = \hbar^2 k_0^2 / 2m^*$ (summarized in Supplementary Note 4); consequently, the Rashba splitting parameter α can be deduced with $\alpha = 2\Delta/k_0$ and the results are shown in Fig. 1f.

The spin splitting of helical excitons at the band extrema is the ‘smoking gun’ evidence for Rashba splitting and it is observed for the first time in 2D complex halide perovskites. The Rashba parameter decreases monotonously with the increase the n of Iodide (Fig. 1f), indicating that the Rashba splitting is highly dependent on the QW thickness and electronic structure. We also find that the Rashba parameter reduces faster for higher n Iodides, suggesting that the strength of Rashba splitting can also be elevated by the internal electric field formed by the polar structure. Note that the probing depth of a photon at the energy range of helical excitons is only tenths of nanometers (see Supplementary Fig. S18) and the XAS technique is also sensitive within tenth of nanometers, these support that the huge Rashba splitting is mostly from the surface effect. The Rashba splitting energy $\Delta_{\text{SOC}} = 115$ meV and Rashba parameter $\alpha = 2.66$ eV·Å in $n=1$ Iodide are comparable with the highest values reported, rendering them promising for spintronics.

Methods

Synthesis of 2D lead RPP single crystals. $(\text{CH}_3(\text{CH}_2)_3\text{NH}_3)_2(\text{CH}_3\text{NH}_3)_{n-1}\text{Pb}_n\text{I}_{3n+1}$ ($n=1-4$) single crystals were synthesized using three solid precursors—PbO, $\text{C}_4\text{H}_9\text{NH}_3\text{I}$ (BAI) and $\text{CH}_3\text{NH}_3\text{I}$ (MAI)—via a temperature-programmed solution precipitation method. The detail sample synthesis can be found in Ref. 7.

Spectroscopic ellipsometry measurement. The ellipsometry studies were carried out on J. A. Woollam ellipsometer which is monochromator based with photon energies ranging from 0.6 to 6.5 eV. Spectroscopic ellipsometry directly measures the changes of the polarization states, which can be expressed by two parameters ψ and Δ . Then the Fresnel

reflection coefficient ratio (ρ) between the two polarized (s - and p -) (r_p and r_s) light can be obtained by calculating the equation as following:

$$\rho = r_p / r_s = \tan \psi e^{i\Delta}, \quad (4)$$

where Δ is the change in phase and ψ is the intensity ratio for p - and s - components of the light after it has interacted with the sample. For the bulk materials, the real and imaginary parts of the complex dielectric function ε_1 and ε_2 can be directly extracted from the Fresnel equations, which are defined as

$$r_p^{ab} = \frac{n_b \cos \theta_a - n_a \cos \theta_b}{n_b \cos \theta_a + n_a \cos \theta_b} \quad (5)$$

$$r_s^{ab} = \frac{n_a \cos \theta_a - n_b \cos \theta_b}{n_a \cos \theta_a + n_b \cos \theta_b}. \quad (6)$$

$$\sqrt{\varepsilon(\omega)} = n(\omega) \quad (7)$$

where n and θ represent the complex refractive index and incidence (transmission) angles, respectively. a and b signify the ambience and sample for the modeling.

Synchrotron radiation based X-ray diffraction measurement. (θ - 2θ) measurements were carried out at the X-ray Demonstration and Development (XDD) beamline (Singapore Synchrotron Light Source, SSLS) which was equipped with a Huber 4-circle system diffractometer having a high precision of 0.0001° step size for ω and 2θ acquisitions. The incident x-ray having a wavelength of 1.5406\AA (8.048 keV) and spot-size of $0.5\text{ mm} \times 0.5\text{ mm}$ with angular divergence of 0.005° after passing through a Si(111) channel-cut monochromator was used.

Angle-dependence X-ray absorption spectra at the C K -edges. X-ray absorption spectroscopy measurements were performed at the SINS beamline of SSLS. The energy resolution was set $\sim 0.1\text{ eV}$. The C K -edge absorption data are collected in total electron yield (TEY) mode monitoring total current. The base pressure in the UHV chamber is maintained at $\sim 2 \times 10^{-10}$ mbar throughout the measurements.

Acknowledgment: X.C and K. L contributed equally to this work. The authors thank Z. Li, E. Chew, H. Miao, W. Wong, W. Zaw, and C. Lim for technical supports. This work was supported by the Singapore National Research Foundation under its Competitive Research Funding (NRF-CRP15-2015-01), MOE-AcRF Tier-2 (MOE2017-T2-1-135, MOE2018-T2-2-117, MOE2019-T2-1-037 and MOE2018-T2-2-117), MOE-AcRF Tier-1 (R-144-000-423-114, R-144-000-423-114 and R-144-000-379-114), HU-NUS (R-144-000-400-133), and NUS Core SupportC-380-003-001. The authors would also like to acknowledge the Singapore Synchrotron Light Source (SSLS) for providing the facilities necessary for conducting the research. The SSLS is a National Research Infrastructure under the National Research Foundation Singapore.

Author Contributions X.C., K.P.L and A.R. conceived the idea. X.C. and A.R. performed spectroscopic ellipsometry measurements and analysis. X.C, X.Y and A.R. performed X-ray absorption measurements and analysis. X.C. and P.Y. performed XRD

measurements. K.L. prepared samples. X.C. and A.R. analyze all data comprehensively and write paper with inputs from all other co-authors. A.R. leads the project.

FIGURE CAPTIONS

Figure 1 | Electronic Rashba effect and dielectric function of layered hybrid RPPs. a and **b** Schematic of band structure and the electron transport path at the band extrema of SOC RPPs with weak and strong Rashba splitting, respectively. The spin texture χ indicates spin vortex direction with its signs denoted as +1 (spin rotation in “counterclockwise”) and -1 (clockwise). Both spin-allowed (\surd) and -forbidden (\times) transitions are marked. **c** and **d** are imaginary part and real part of dielectric function of $n=1$ Iodide, respectively, measured at 78 K. The four helical exciton peaks (I II III and IV) are associated with the spin-allowed and -forbidden transitions in **b**. The zoom-in shows the energy position of band-to-band transitions. **e**, Band-gap energies for various QW thicknesses to infinite. The diamonds indicate the experimental data and the red line corresponds to the model fitting. **f**, The calculated Rashba parameters α for both CB and VB.

Figure 2 | Experimental and fitted results of temperature dependence of dielectric functions. a, c and **b, d** are the temperature dependence of real and imaginary part of dielectric functions, respectively. The four helical excitons and band-to-band transitions can be well identified. **d** to **h** are the fitting parameters of helical excitons, including integrated peak intensity **d**, peak energy **f**, Rashba splitting energy **j** and total peak intensity **k**.

Figure 3 | Rashba splitting on both CB and VB with increasing n of RPPs from 1 to 4. a and **b** are the n dependence of real and imaginary part of dielectric functions, respectively. **c**, Peak energy position of co-helical exciton of RPPs for $n= 1$ to 4. **d**, n

dependence of Rashba splitting energies on both CB and VB at room temperature. **e**, Diagram shows the QW confinement effect on the Rashba splitting and how they are reflected in band structure.

Figure 4 | Molecular orientation and internal electric field between organic and inorganic frameworks. **a**, Schematic of the interaction of linearly polarization light with molecule orbitals; the in-plane and out-of-plane molecular orbital can be detected by in-plane and out-of-plane linearly polarization lights, respectively. **b**, Normalized XAS spectra of $n=1$ to 4 RPPs measured at both normal (NI) and grazing (GI) incidence. The XLD spectral ($I_{GI}-I_{NI}$) for each sample are shown. **c**, C $1s$ and Pb $4f$ core-level spectra for the $n=1$ to 4 RPPs, shifted to align the C $1s$ peaks. The inset shows the peak shift of Pb $4f$. The C $1s$ and Pb $4f$ have been shifted slightly so that all C $1s$ peaks are aligned at 285 eV as a means of visualizing the separation between the C $1s$ and Pb $4f$ peaks, that is to say, we can estimate the change of potential gradient by this energy separation³⁹. **d**, The summary of energy shift of Pb $4f$ as a reference of 3D ($n=\infty$).

FIGURES

Figure 1

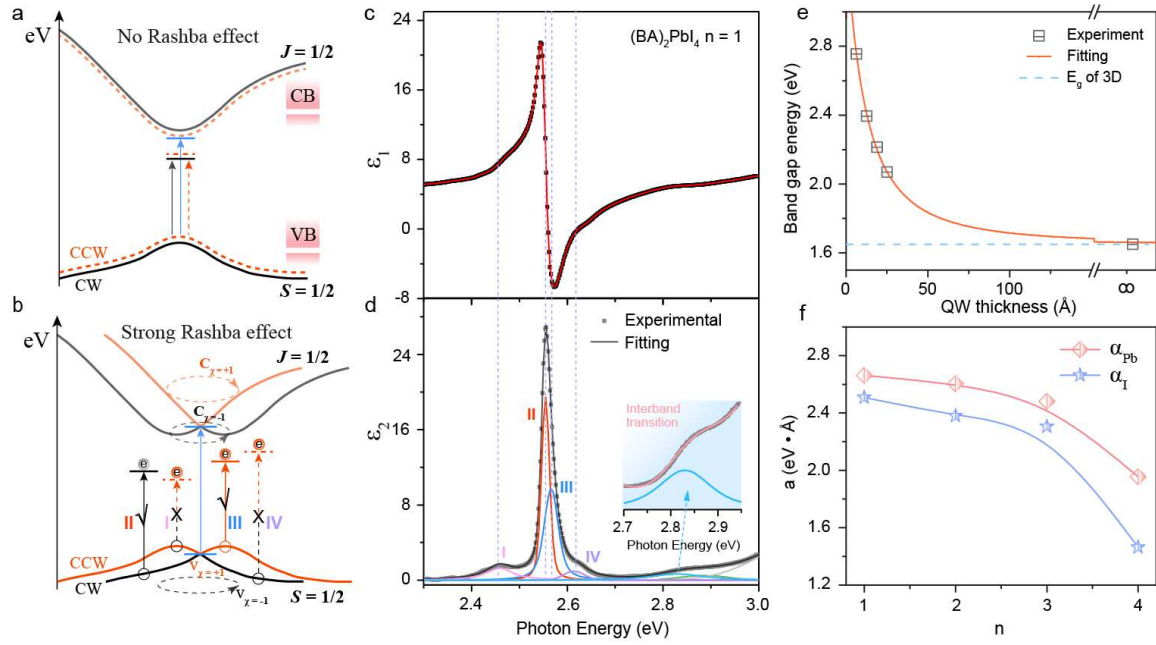


Figure 2

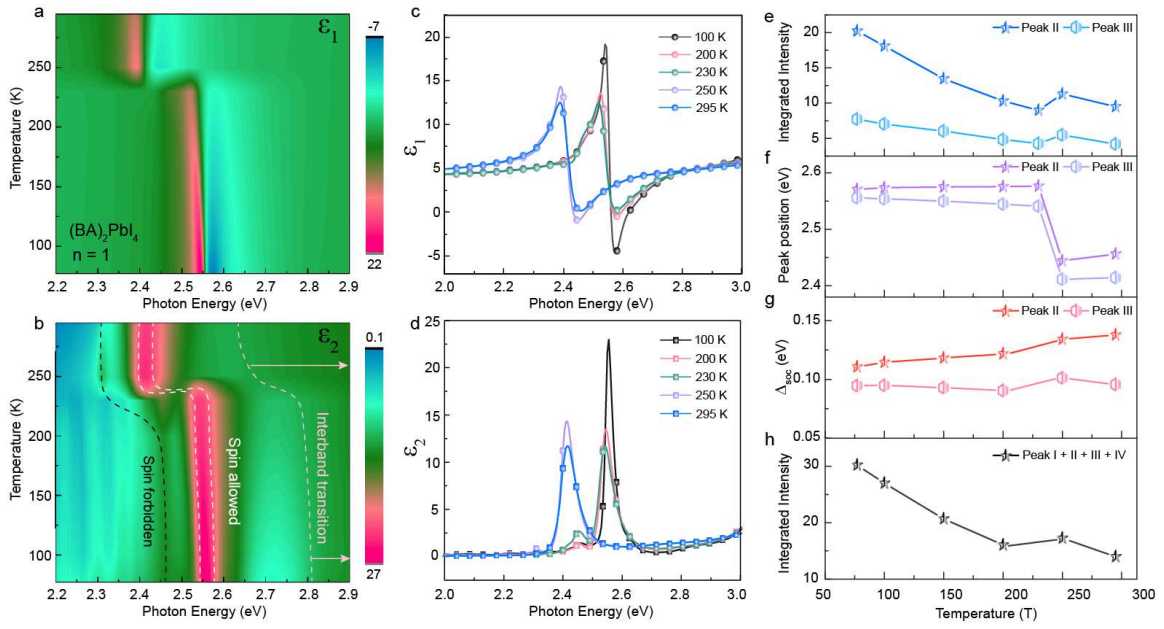


Figure 3

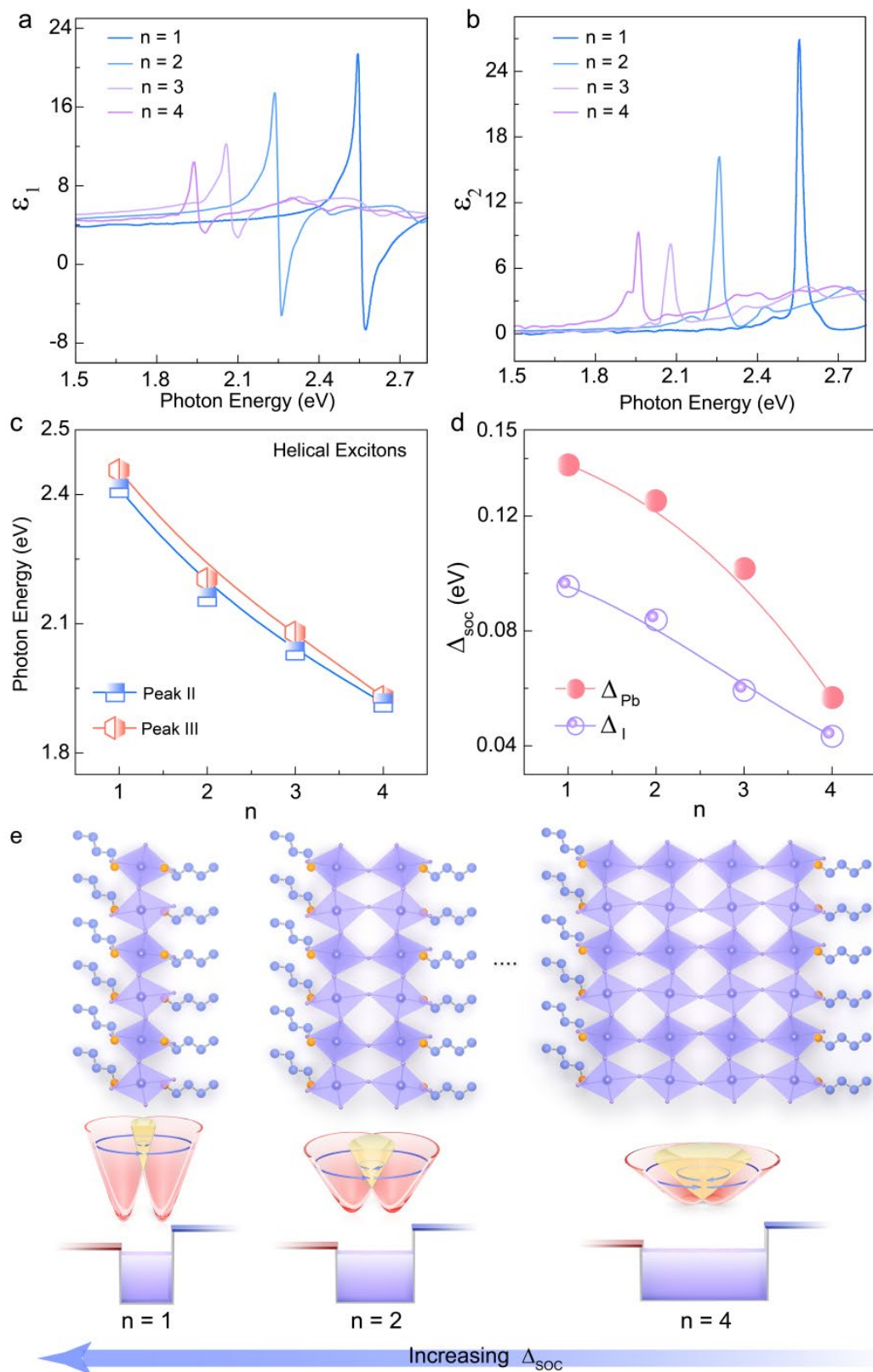
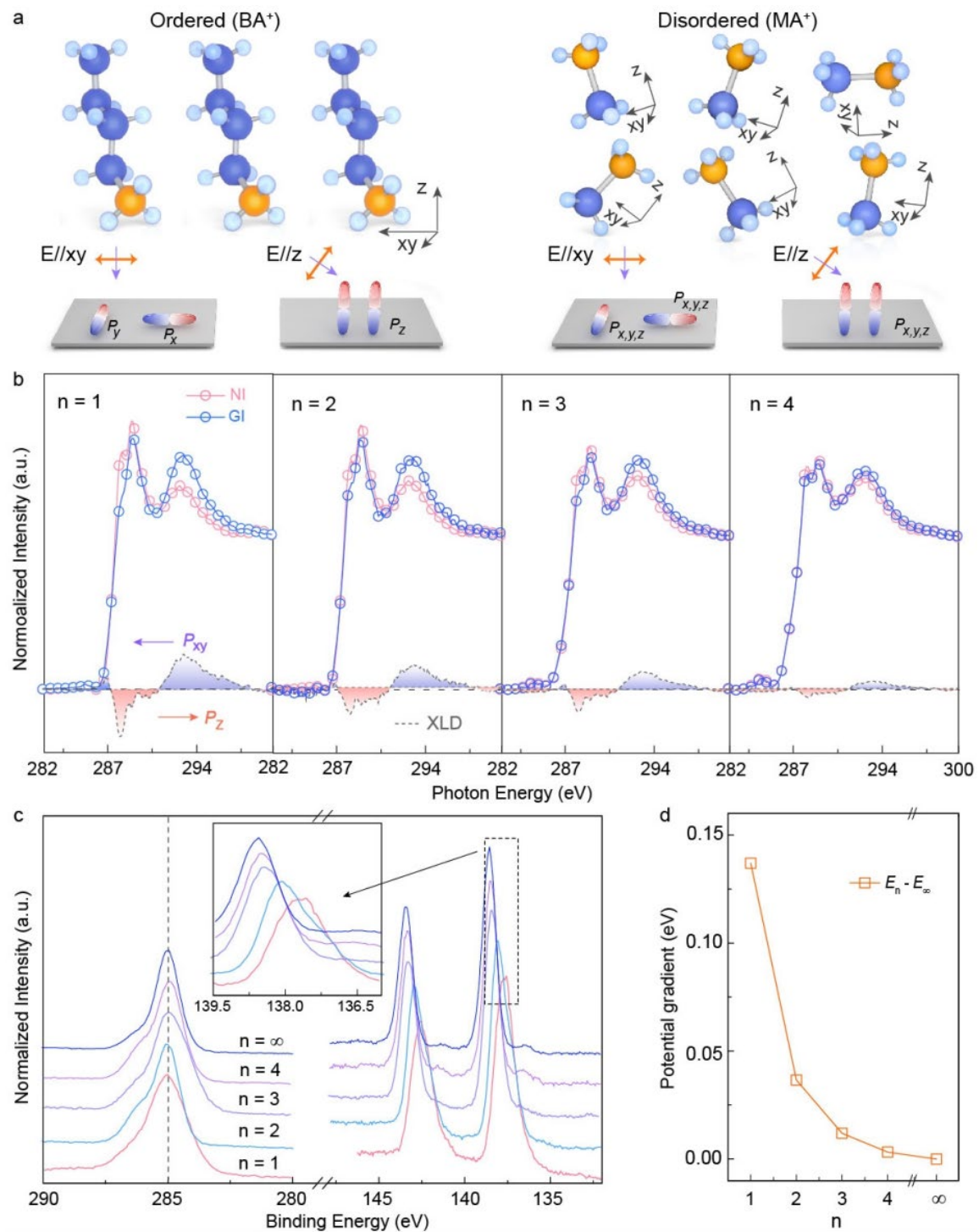


Figure 4



References

1. Kim, M., Im, J., Freeman, A. J., Ihm, J. & Jin, H. Switchable $S=1/2$ and $J=1/2$ Rashba bands in ferroelectric halide perovskites. *Proc. Natl Acad. Sci. USA* 111, 6900 (2014).
2. Zheng, F., Tan, L. Z., Liu, S. & Rappe, A. M. Rashba spin-orbit coupling enhanced carrier lifetime in $\text{CH}_3\text{NH}_3\text{PbI}_3$. *Nano Lett.* 15, 7794 (2015).
3. Niesner, D., Wilhelm, M., Levchuk, I., Osvet, A., Shrestha, S., Batentschuk, M., Brabec, C. & Fauster, T. Giant Rashba splitting in $\text{CH}_3\text{NH}_3\text{PbBr}_3$ organic-inorganic perovskite. *Phys. Rev. Lett.* 117, 126401 (2016).
4. Stranks, S. D. & Plochocka, P. The influence of the Rashba effect. *Nat. Mater.* 17, 381 (2018).
5. Liu, X., Chanana, A., Huynh, U., Xue, F., Haney, P., Blair, S., Jiang, X. & Vardeny, Z. Circular photogalvanic spectroscopy of Rashba splitting in 2D hybrid organic-inorganic perovskite multiple quantum wells. *Nat. Commun.* 11, 1 (2020).
6. Liu, Z., Vaswani, C., Yang, X., Zhao, X., Yao, Y., Song, Z., Cheng, D., Shi, Y., Luo, L. & Mudiyansele, D.-H. Ultrafast Control of Excitonic Rashba Fine Structure by Phonon Coherence in the Metal Halide Perovskite $\text{CH}_3\text{NH}_3\text{PbI}_3$. *Phys. Rev. Lett.* 124, 157401 (2020).
7. Leng, K., Abdelwahab, I., Verzhbitskiy, I., Telychko, M., Chu, L., Fu, W., Chi, X., Guo, N., Chen, Z. & Chen, Z. Molecularly thin two-dimensional hybrid perovskites with tunable optoelectronic properties due to reversible surface relaxation. *Nat. Mater.* 17, 908 (2018).
8. Chen, Y., Sun, Y., Peng, J., Tang, J., Zheng, K. & Liang, Z. 2D Ruddlesden-Popper perovskites for optoelectronics. *Adv. Mater.* 30, 1703487 (2018).
9. Ishihara, T., Takahashi, J. & Goto, T. Optical properties due to electronic transitions in two-dimensional semiconductors $(\text{C}_n\text{H}_{2n+1}\text{NH}_3)_2\text{PbI}_4$. *Phys. Rev. B* 42, 11099 (1990).
10. Stoumpos, C. C., Cao, D. H., Clark, D. J., Young, J., Rondinelli, J. M., Jang, J. I., Hupp, J. T. & Kanatzidis, M. G. Ruddlesden-Popper hybrid lead iodide perovskite 2D homologous semiconductors. *Chem. Mater.* 28, 2852 (2016).
11. Pedesseau, L., Saponi, D., Traore, B., Robles, R., Fang, H.-H., Loi, M. A., Tsai, H., Nie, W., Blancon, J.-C. & Neukirch, A. Advances and promises of layered halide hybrid perovskite semiconductors. *ACS Nano* 10, 9776 (2016).
12. Blancon, J.-C., Tsai, H., Nie, W., Stoumpos, C. C., Pedesseau, L., Katan, C., Kepenekian, M., Soe, C. M. M., Appavoo, K. & Sfeir, M. Y. Extremely efficient internal exciton dissociation through edge states in layered 2D perovskites. *Science* 355, 1288 (2017).
13. Borriello, I., Cantele, G. & Ninno, D. Ab initio investigation of hybrid organic-inorganic perovskites based on tin halides. *Phys. Rev. B* 77, 235214 (2008).
14. Lanty, G., Jemli, K., Wei, Y., Leymarie, J., Even, J., Lauret, J.-S. & Deleporte, E. Room-temperature optical tunability and inhomogeneous broadening in 2D-layered organic-inorganic perovskite pseudobinary alloys. *J. Phys. Chem. Lett.* 5, 3958 (2014).
15. Dou, L., Wong, A. B., Yu, Y., Lai, M., Kornienko, N., Eaton, S. W., Fu, A., Bischak, C. G., Ma, J. & Ding, T. Atomically thin two-dimensional organic-inorganic hybrid perovskites. *Science* 349, 1518 (2015).
16. Even, J., Pedesseau, L., Jancu, J.-M. & Katan, C. Importance of spin-orbit coupling in hybrid organic/inorganic perovskites for photovoltaic applications. *J. Phys. Chem. Lett.* 4, 2999 (2013).
17. Brivio, F., Butler, K. T., Walsh, A. & Van Schilfgaarde, M. Relativistic quasiparticle self-consistent electronic structure of hybrid halide perovskite photovoltaic absorbers. *Phys. Rev. B* 89, 155204 (2014).

18. Rashba, E. I. Properties of semiconductors with an extremum loop. I. Cyclotron and combinational resonance in a magnetic field perpendicular to the plane of the loop. *Phys. Solid State* 2, 1109 (1960).
19. Zhai, Y., Baniya, S., Zhang, C., Li, J., Haney, P., Sheng, C.-X., Ehrenfreund, E. & Vardeny, Z. V. Giant Rashba splitting in 2D organic-inorganic halide perovskites measured by transient spectroscopies. *Sci. Adv.* 3, e1700704 (2017).
20. Becker, M. A., Vaxenburg, R., Nedelcu, G., Sercel, P. C., Shabaev, A., Mehl, M. J., Michopoulos, J. G., Lambrakos, S. G., Bernstein, N. & Lyons, J. L. Bright triplet excitons in caesium lead halide perovskites. *Nature* 553, 189 (2018).
21. Niesner, D., Hauck, M., Shrestha, S., Levchuk, I., Matt, G. J., Osvet, A., Batentschuk, M., Brabec, C., Weber, H. B. & Fauster, T. Structural fluctuations cause spin-split states in tetragonal $(\text{CH}_3\text{NH}_3)\text{PbI}_3$ as evidenced by the circular photogalvanic effect. *Proc. Natl Acad. Sci. USA* 115, 9509 (2018).
22. Li, J. & Haney, P. M. Circular photogalvanic effect in organometal halide perovskite $\text{CH}_3\text{NH}_3\text{PbI}_3$. *Appl. Phys. Lett.* 109, 193903 (2016).
23. Price, M. B., Butkus, J., Jellicoe, T. C., Sadhanala, A., Briane, A., Halpert, J. E., Broch, K., Hodgkiss, J. M., Friend, R. H. & Deschler, F. Hot-carrier cooling and photoinduced refractive index changes in organic-inorganic lead halide perovskites. *Nat. Commun.* 6, 1 (2015).
24. Santoso, I., Ku, W., Shirakawa, T., Neuber, G., Yin, X., Enoki, M., Fujita, M., Liang, R., Venkatesan, T. & Sawatzky, G. A. Unraveling local spin polarization of Zhang-Rice singlet in lightly hole-doped cuprates using high-energy optical conductivity. *Phys. Rev. B* 95, 165108 (2017).
25. Bousquet, E., Dawber, M., Stucki, N., Lichtensteiger, C., Hermet, P., Gariglio, S., Triscone, J.-M. & Ghosez, P. Improper ferroelectricity in perovskite oxide artificial superlattices. *Nature* 452, 732 (2008).
26. Lee, H. N., Christen, H. M., Chisholm, M. F., Rouleau, C. M. & Lowndes, D. H. Strong polarization enhancement in asymmetric three-component ferroelectric superlattices. *Nature* 433, 395 (2005).
27. Zheng, H., Wang, J., Lofland, S., Ma, Z., Mohaddes-Ardabili, L., Zhao, T., Salamanca-Riba, L., Shinde, S., Ogale, S. & Bai, F. Multiferroic $\text{BaTiO}_3\text{-CoFe}_2\text{O}_4$ nanostructures. *Science* 303, 661 (2004).
28. Chi, X., Wang, H., Guo, R., Whitcher, T. J., Yu, X., Yang, P., Yan, X., Breese, M. B., Loh, K. P. & Chen, J. Unusual hole and electron midgap states and orbital reconstructions induced huge Ferroelectric Tunneling Electroresistance in $\text{BaTiO}_3/\text{SrTiO}_3$. *Nano Lett.* 20, 1101 (2020).
29. Lee, J., Schober, G., Bahramy, M., Murakawa, H., Onose, Y., Arita, R., Nagaosa, N. & Tokura, Y. Optical response of relativistic electrons in the polar BiTeI semiconductor. *Phys. Rev. Lett.* 107, 117401 (2011).
30. Shao, Y., Rudenko, A., Hu, J., Sun, Z., Zhu, Y., Moon, S., Millis, A., Yuan, S., Lichtenstein, A. & Smirnov, D. Electronic correlations in nodal-line semimetals. *Nat. Phys.* 1 (2020).
31. Billing, D. G. & Lemmerer, A. Synthesis, characterization and phase transitions in the inorganic-organic layered perovskite-type hybrids $[(\text{C}_n\text{H}_{2n+1}\text{NH}_3)_2\text{PbI}_4]$, $n = 4, 5$ and 6 . *Acta Cryst.* B63, 735 (2007).
32. Eskes, H., Meinders, M. & Sawatzky, G. Anomalous transfer of spectral weight in doped strongly correlated systems. *Phys. Rev. Lett.* 67, 1035 (1991).
33. Phillips, P. Colloquium: Identifying the propagating charge modes in doped Mott insulators. *Rev. Modern Phys.* 82, 1719 (2010).
34. Ohta, Y., Tsutsui, K., Koshibae, W., Shimozato, T. & Maekawa, S. Evolution of the in-gap state in high-T c cuprates. *Phys. Rev. B* 46, 14022 (1992).

35. Rusydi, A., Rauer, R., Neuber, G., Bastjan, M., Mahns, I., Müller, S., Saichu, P., Schulz, B., Singer, S. & Lichtenstein, A. Metal-insulator transition in manganites: changes in optical conductivity up to 22 eV. *Phys. Rev. B* 78, 125110 (2008).
36. Chi, X., Huang, Z., Asmara, T. C., Han, K., Yin, X., Yu, X., Diao, C., Yang, M., Schmidt, D. & Yang, P. Large enhancement of 2D electron gases mobility induced by interfacial localized electron screening effect. *Adv. Mater.* 30, 1707428 (2018).
37. Nakagawa, N., Hwang, H. Y. & Muller, D. A. Why some interfaces cannot be sharp. *Nat. Mater.* 5, 204 (2006).
38. Even, J., Pedesseau, L. & Katan, C. Understanding quantum confinement of charge carriers in layered 2D hybrid perovskites. *ChemPhysChem* 15, 3733 (2014).
39. Comes, R. & Chambers, S. Interface Structure, Band Alignment, and Built-In Potentials at LaFeO₃/n-SrTiO₃ Heterojunctions. *Phys. Rev. Lett.* 117, 226802 (2016).

Figures

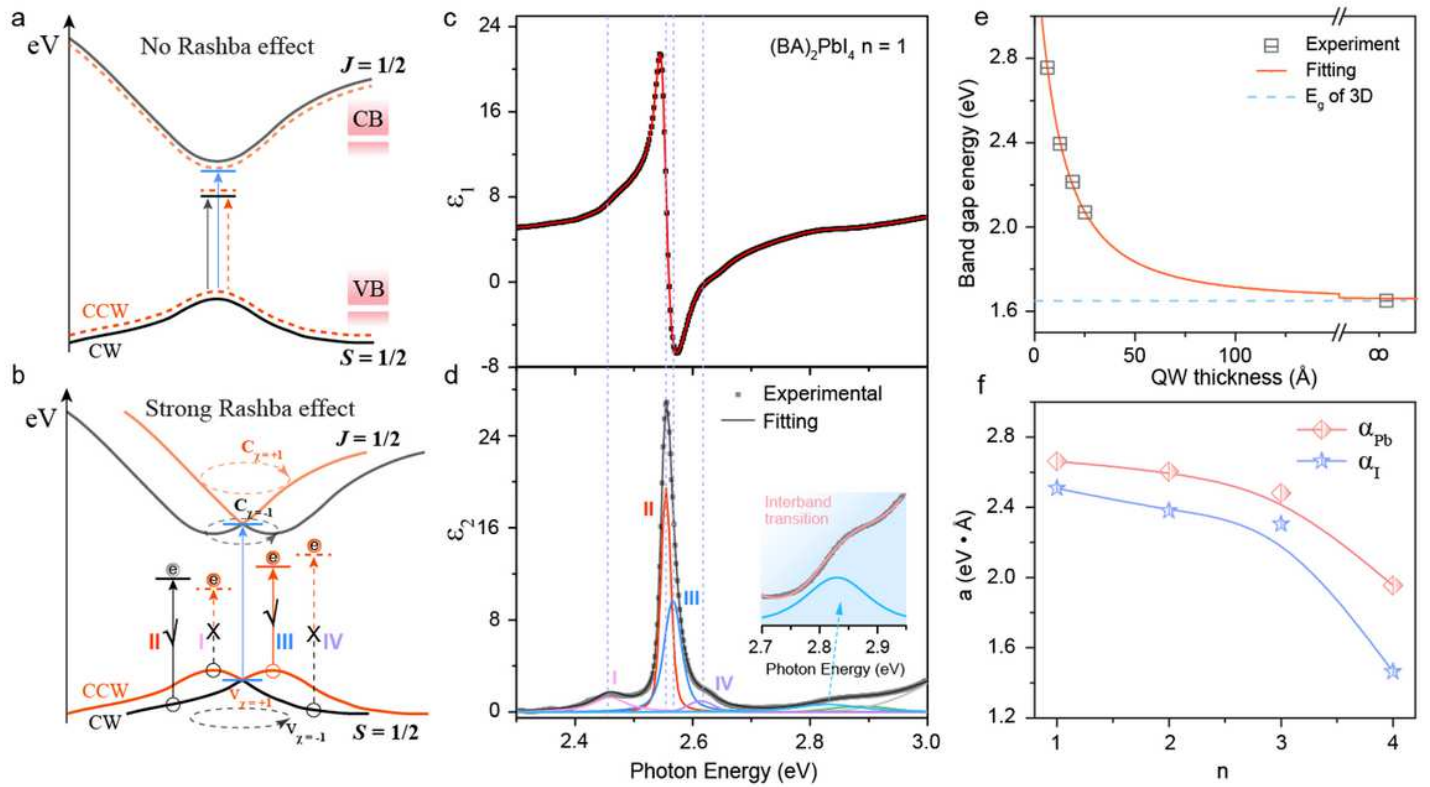


Figure 1

Electronic Rashba effect and dielectric function of layered hybrid RPPs. a and b Schematic of band structure and the electron transport path at the band extrema of SOC RPPs with weak and strong Rashba splitting, respectively. The spin texture χ indicates spin vortex direction with its signs denoted as +1 (spin rotation in "counterclockwise") and -1 (clockwise). Both spin-allowed (\boxtimes) and -forbidden (\times) transitions are marked. c and d are imaginary part and real part of dielectric function of $n=1$ Iodide, respectively, measured at 78 K. The four helical exciton peaks (I II III and IV) are associated with the spin-allowed and -forbidden transitions in b. The zoom-in shows the energy position of band-to-band transitions. e, Band-gap energies for various QW thicknesses to infinite. The diamonds indicate the experimental data and the red line corresponds to the model fitting. f, The calculated Rashba parameters α for both CB and VB.

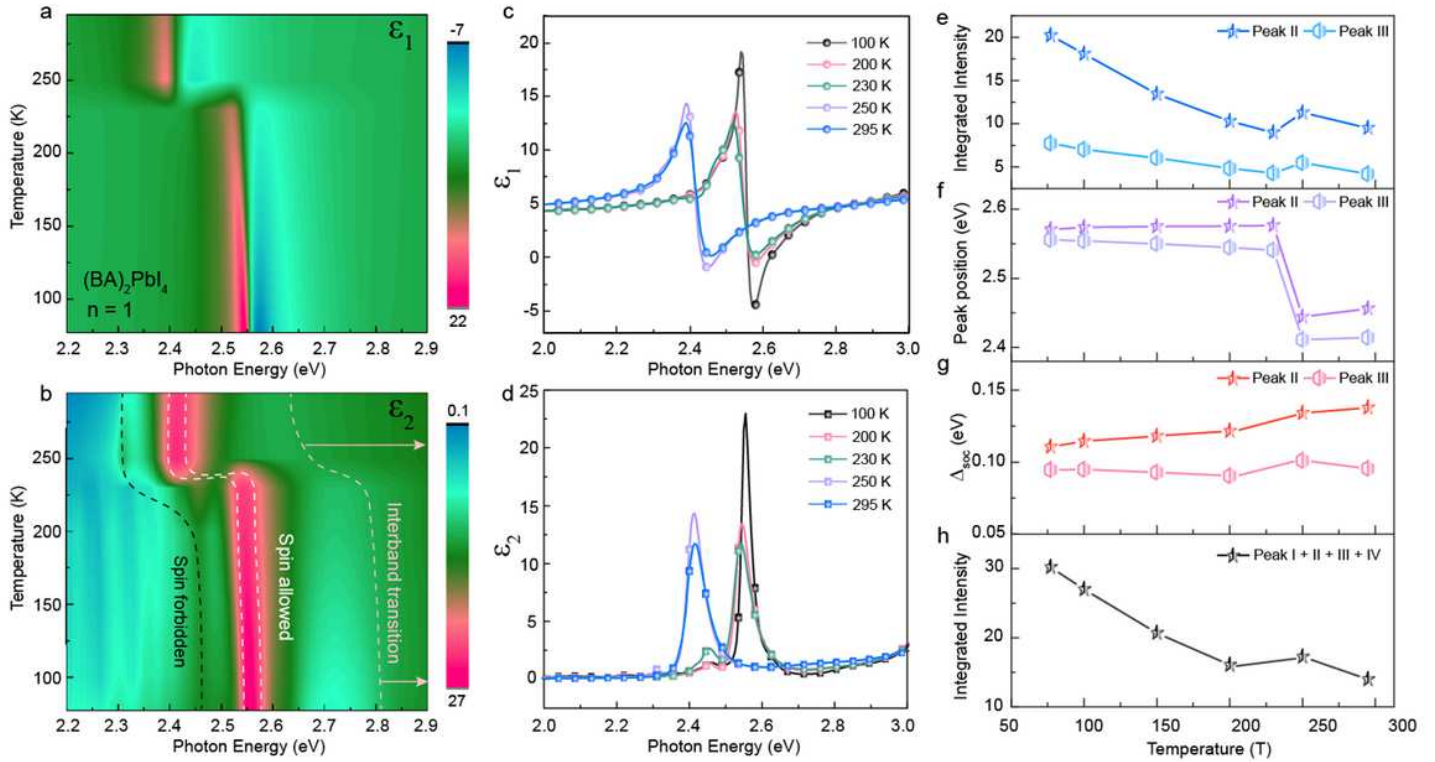


Figure 2

Experimental and fitted results of temperature dependence of dielectric functions. a, c and b, d are the temperature dependence of real and imaginary part of dielectric functions, respectively. The four helical excitons and band-to-band transitions can be well identified. d to h are the fitting parameters of helical excitons, including integrated peak intensity d, peak energy f, Rashba splitting energy j and total peak intensity k.

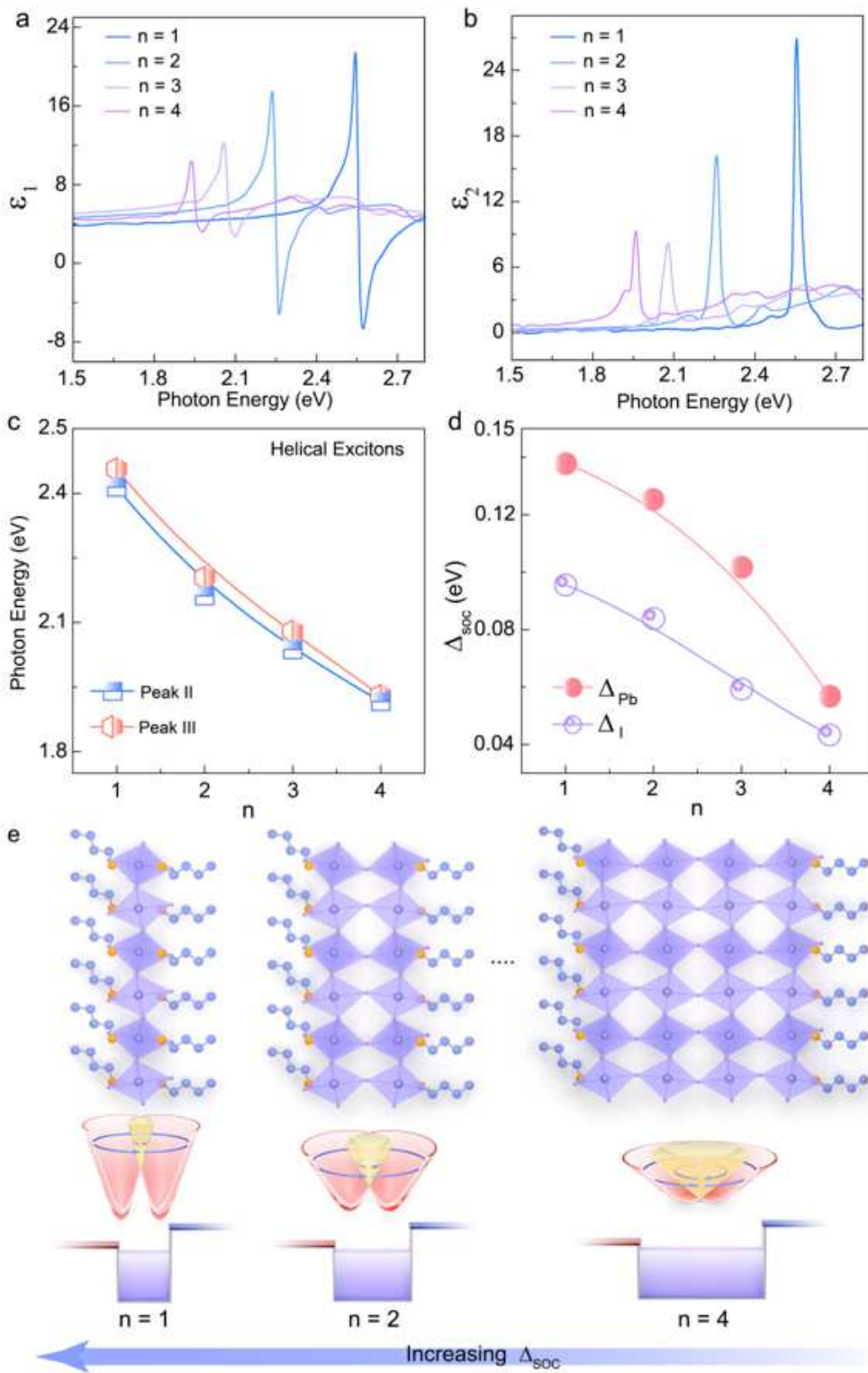


Figure 3

Rashba splitting on both CB and VB with increasing n of RPPs from 1 to 4. a and b are the n dependence of real and imaginary part of dielectric functions, respectively. c, Peak energy position of co-helical exciton of RPPs for $n=1$ to 4. d, n dependence of Rashba splitting energies on both CB and VB at room temperature. e, Diagram shows the QW confinement effect on the Rashba splitting and how they are reflected in band structure.

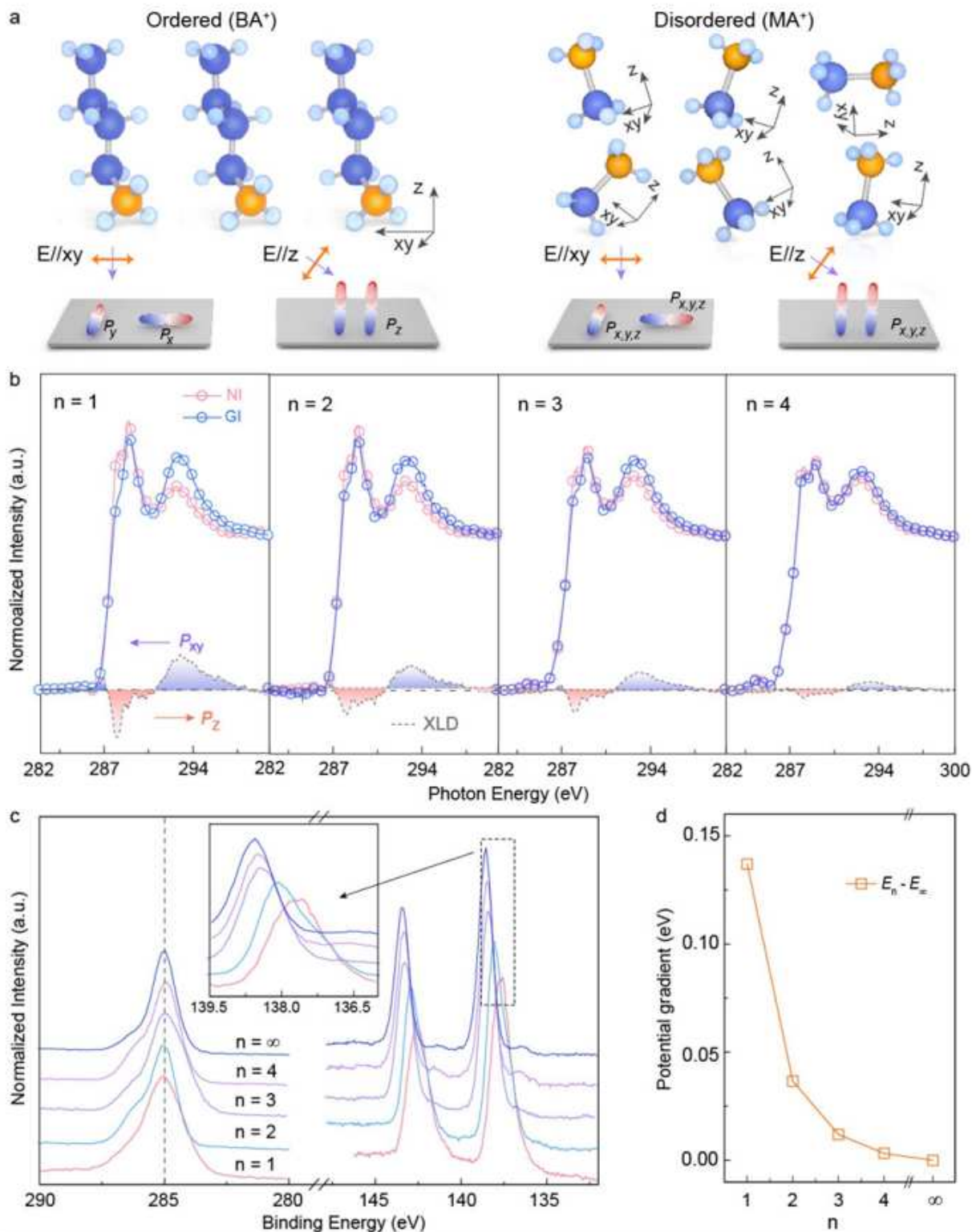


Figure 4

Molecular orientation and internal electric field between organic and inorganic frameworks. a, Schematic of the interaction of linearly polarization light with molecule orbitals; the in-plane and out-of-plane molecular orbital can be detected by in-plane and out-of-plane linearly polarization lights, respectively. b, Normalized XAS spectra of n=1 to 4 RPPs measured at both normal (NI) and grazing (GI) incidence. The XLD spectral (IGI-INI) for each sample are shown. c, C 1s and Pb 4f core-level spectra for the n=1 to 4

RPPs, shifted to align the C 1s peaks. The inset shows the peak shift of Pb 4f. The C 1s and Pb 4f have been shifted slightly so that all C 1s peaks are aligned at 285 eV as a means of visualizing the separation between the C 1s and Pb 4f peaks, that is to say, we can estimate the change of potential gradient by this energy separation³⁹. d, The summary of energy shift of Pb 4f as a reference of 3D ($n=\infty$).

Supplementary Files

This is a list of supplementary files associated with this preprint. Click to download.

- [SupplementaryMaterials.docx](#)